Behavioral/Cognitive

Ultra-High-Field Neuroimaging Reveals Fine-Scale Processing for 3D Perception

Adrian K. T. Ng,[1,4*] **Ke Jia,**[1*] **Nuno R. Goncalves,**[1] **Elisa Zamboni,**[1] **Valentin G. Kemper,**[2,3] **Rainer Goebel,**[2,3] **Andrew E. Welchman,**[1] **and Zoe Kourtzi**[1]

[1]Department of Psychology, University of Cambridge, Cambridge CB2 3EB, United Kingdom, [2]Department of Cognitive Neuroscience, Faculty of Psychology and Neuroscience, Maastricht University, 6200 MD Maastricht, The Netherlands, [3]Department of Cognitive Neuroscience, Maastricht Brain Imaging Centre, Maastricht University, 6200 MD Maastricht, The Netherlands, and [4]Department of Industrial and Manufacturing Systems Engineering, University of Hong Kong, Hong Kong S.A.R., China

Binocular disparity provides critical information about three-dimensional (3D) structures to support perception and action. In the past decade significant progress has been made in uncovering human brain areas engaged in the processing of binocular disparity signals. Yet, the fine-scale brain processing underlying 3D perception remains unknown. Here, we use ultra-high-field (7T) functional imaging at submillimeter resolution to examine fine-scale BOLD fMRI signals involved in 3D perception. In particular, we sought to interrogate the local circuitry involved in disparity processing by sampling fMRI responses at different positions relative to the cortical surface (i.e., across cortical depths corresponding to layers). We tested for representations related to 3D perception by presenting participants (male and female, $N = 8$) with stimuli that enable stable stereoscopic perception [i.e., correlated random dot stereograms (RDS)] versus those that do not (i.e., anticorrelated RDS). Using multivoxel pattern analysis (MVPA), we demonstrate cortical depth-specific representations in areas V3A and V7 as indicated by stronger pattern responses for correlated than for anticorrelated stimuli in upper rather than deeper layers. Examining informational connectivity, we find higher feedforward layer-to-layer connectivity for correlated than anticorrelated stimuli between V3A and V7. Further, we observe disparity-specific feedback from V3A to V1 and from V7 to V3A. Our findings provide evidence for the role of V3A as a key nexus for disparity processing, which is implicated in feedforward and feedback signals related to the perceptual estimation of 3D structures.

Key words: **binocular disparity; depth perception; functional connectivity; ultra-high-field fMRI; visual cortex**

Significance Statement

Binocular vision plays a significant role in supporting our interactions with the surrounding environment. The fine-scale neural mechanisms that underlie the brain's skill in extracting 3D structures from binocular signals are poorly understood. Here, we capitalize on recent advances in ultra-high-field functional imaging to interrogate human brain circuits involved in 3D perception at submillimeter resolution. We provide evidence for the role of area V3A as a key nexus for disparity processing, which is implicated in feedforward and feedback signals related to the perceptual estimation of 3D structures from binocular signals. These fine-scale measurements help bridge the gap between animal neurophysiology and human fMRI studies investigating cross-scale circuits, from micro circuits to global brain networks for 3D perception.

Introduction

Binocular vision provides humans with two slightly different views of the world (i.e., binocular disparity) from which the brain can triangulate the structure of the environment. The process of inferring 3D structures from differences in the signals registered in the two eyes is the result of an unknown series of computations that starts in the primary visual cortex—the first point of integration of signals from the two eyes. Human neuroimaging studies have revealed widespread responses to binocular signals in the occipitoparietal regions (Bridge and Parker, 2007; Welchman, 2016) with the strongest modulation of brain activity by binocular signals in areas V3A and V7 (Backus et al., 2001;

Received Dec. 22, 2020; revised June 8, 2021; accepted July 7, 2021.

Author contributions: N.R.G., V.G.K., R.G., A.E.W., and Z.K. designed research; N.R.G., E.Z., and V.G.K. performed research; A.K.T.N., K.J., and E.Z. analyzed data; A.K.T.N., K.J., A.E.W., and Z.K. wrote the paper.

This work was funded by grants to Z.K. from the Biotechnology and Biological Sciences Research Council (H012508 and BB/P021255/1), the Wellcome Trust (205067/Z/16/Z) and the European Union Horizon 2020 Research and Innovation Program under grant agreements 765121 and 840271. We thank Christopher Wiggins, Esther Steijvers (Scannexus) and Federico De Martino (University of Maastricht) for technical support.

*A.K.T.N. and K.J. contributed equally to this work.

The authors declare no competing financial interests.

Correspondence should be addressed to Zoe Kourtzi at zk240@cam.ac.uk.

https://doi.org/10.1523/JNEUROSCI.0065-21.2021

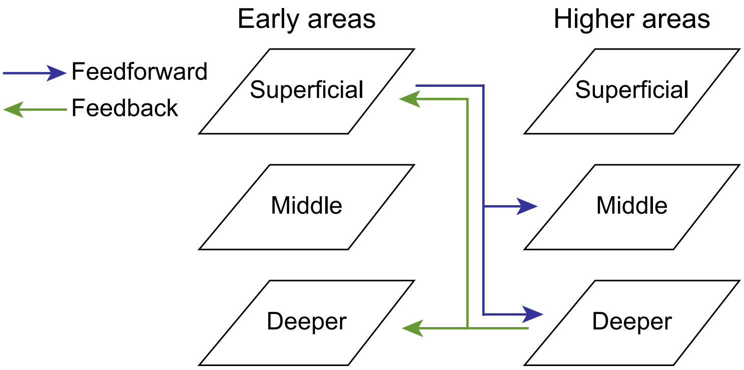

Figure 1. fMRI circuits across cortical depth. Schematic representation of feedforward (superficial–middle layers, blue) and feedback (deeper–deeper layers, green) anatomic connectivity between early and higher visual areas based on known anatomic circuits.

Tsao et al., 2003; Preston et al., 2008; Minini et al., 2010; Cottereau et al., 2011; Goncalves et al., 2015; Rideaux and Welchman, 2019; Liu et al., 2020). There is evidence for local clustering of disparity-selective organization in area V3A (Goncalves et al., 2015; Parker et al., 2017; Tootell and Nasr, 2017; Nasr and Tootell, 2020), as well as areas V2 and V3 (Nasr and Tootell, 2018). These findings indicate that parts of the dorsal visual cortex are heavily involved in processing disparity signals. However, the fine-scale processing and interactions among these regions that support our ability to perceive 3D structures remain largely unknown. Our understanding of how disparity signals are processed within and between different cortical regions is limited, with some evidence suggesting local recurrent processing (Tanabe and Cumming, 2014), and other studies pointing to interactions among areas (Cottereau et al., 2014).

Here, we capitalize on recent advances in ultra-high-field (UHF) imaging to examine the local circuitry for disparity processing at a finer scale in the human brain. UHF imaging provides the submillimeter resolution necessary to examine functional activation within a visual area at different positions relative to the cortical surface (i.e., cortical depth) in a noninvasive manner (Goense et al., 2016; Lawrence et al., 2019b). This allows us to test functional connectivity across cortical layers based on known anatomic laminar circuits from electrophysiological studies (Fig. 1; Self et al., 2019). Specifically, sensory input is known to enter the visual cortex from the thalamus at the level of the middle layer (layer 4; Hubel and Wiesel, 1972; Blasdel and Lund, 1983), whereas output information is fed forward from superficial layers (layer 2/3; Livingstone and Hubel, 1984). Feedback information is exchanged primarily between deeper layers (layer 5/6) and from deeper to superficial layers (Rockland and Pandya, 1979). This circuitry motif has been implicated in a range of visual computations revealed through neurophysiological studies (Self et al., 2013) and human fMRI studies that discern signals from different cortical depths to infer feedforward versus feedback processing (Lawrence et al., 2019a; Jia et al., 2020; Zamboni et al., 2020).

Here, we employ submillimeter fMRI to investigate the contribution of feedforward and feedback mechanisms in the visual cortex related to 3D perception. We compare fMRI responses across cortical depths to stimuli that enable stable stereoscopic perception [i.e., correlated random dot stereograms (RDS) vs anticorrelated RDS stimuli that do not support a unified perceptual experience of 3D structures; Fig. 2*A*]. Using multivoxel pattern analysis (MVPA) across cortical depths, we demonstrate cortical depth-specific representations in areas V3A and V7; that is, multivoxel pattern responses were stronger for correlated than anticorrelated stimuli in upper rather than deeper layers. Further, we show higher feedforward connectivity for correlated than anticorrelated stimuli between superficial layers of V3A and middle layers of V7, suggesting that V3A propagates 3D structure information to higher dorsal areas. Finally, we show higher feedback connectivity for correlated than anticorrelated stimuli between deeper layers of V3A and V1 and of V7 and V3A, suggesting top-down influences on binocular disparity processing. Our findings indicate that area V3A is a key nexus for disparity processing, which gates feedforward and feedback interactions to support 3D perception.

Materials and Methods

Participants

Eight healthy volunteers (six female; 22–31 years old) participated in the study. The sample size followed previous 7T fMRI studies (Goncalves et al., 2015, $N = 6$) on binocular disparity using RDS stimuli. Data from one participant were excluded from further analysis because of excessive head movement (higher than 1.5 mm). All participants had normal or corrected-to-normal vision and were screened for stereo deficits before entering the scanner. Participants gave written informed consent and received payment for their participation. The study was approved by the local Ethical Committee of the Faculty of Psychology and Neuroscience at Maastricht University.

Stimuli

The stimuli were random dot stereogram images consisting of black and white dots on a midgray background. Within these patterns we imposed a disparity structure that defined four wedges,, which were either in front or behind the background plane of fixation (Fig. 2*B*). These wedges were only visible once binocular correspondence had been established (Fig. 2*C*–*D*), that is, if viewing the stimuli monocularly only randomly placed dots were apparent within a square region containing the stimulus (side length 8°). The wedges were presented centrally around a circular aperture (diameter 1.2°) containing the fixation marker that was positioned in the plane of the screen (Goncalves et al., 2015). Each wedge subtended 7° in the radial direction and 70° in polar angle. To reduce adaptation effects, we changed the position of the disparity-defined edges of the wedge stimulus across stimulus presentations by randomly rotating the wedge regions clockwise or counterclockwise. The stimuli (wedges and the background) were presented in correlated or anticorrelated form of dense RDS (Preston et al., 2008). For the correlated RDS patterns (Fig. 2*A*), the polarity of the dots presented matched between the eyes (e.g., a black dot in the left eye matched a black dot in the right eye, whereas a white dot in the left eye matched a white dot in the right eye). In the anticorrelated RDS (Fig. 2*A*), we inverted the contrast polarity between the eyes (e.g., a black dot in the left eye matched a white dot in the right eye, and a white dot in the left eye matched a black dot in the right eye). When participants viewed correlated stimuli, they were able to perceive the wedges in front or behind the background. When participants viewed the anticorrelated stimuli, the whole stimulus appeared lustrous, and there was no consistent impression of a 3D structure. The background and fixation target were presented at the plane of the screen (i.e., zero disparity). The wedges were presented at near or far perceived depth corresponding to crossed versus uncrossed disparities [±10 minutes of arc (arcmin) with ±0.5 arcmin jitter, Fig. 2*B*]. In the crossed disparity configuration, the stimulus was closer (near) to the observer than the fixation plane; in the uncrossed disparity configuration, the stimulus was farther (far) from the observer than the

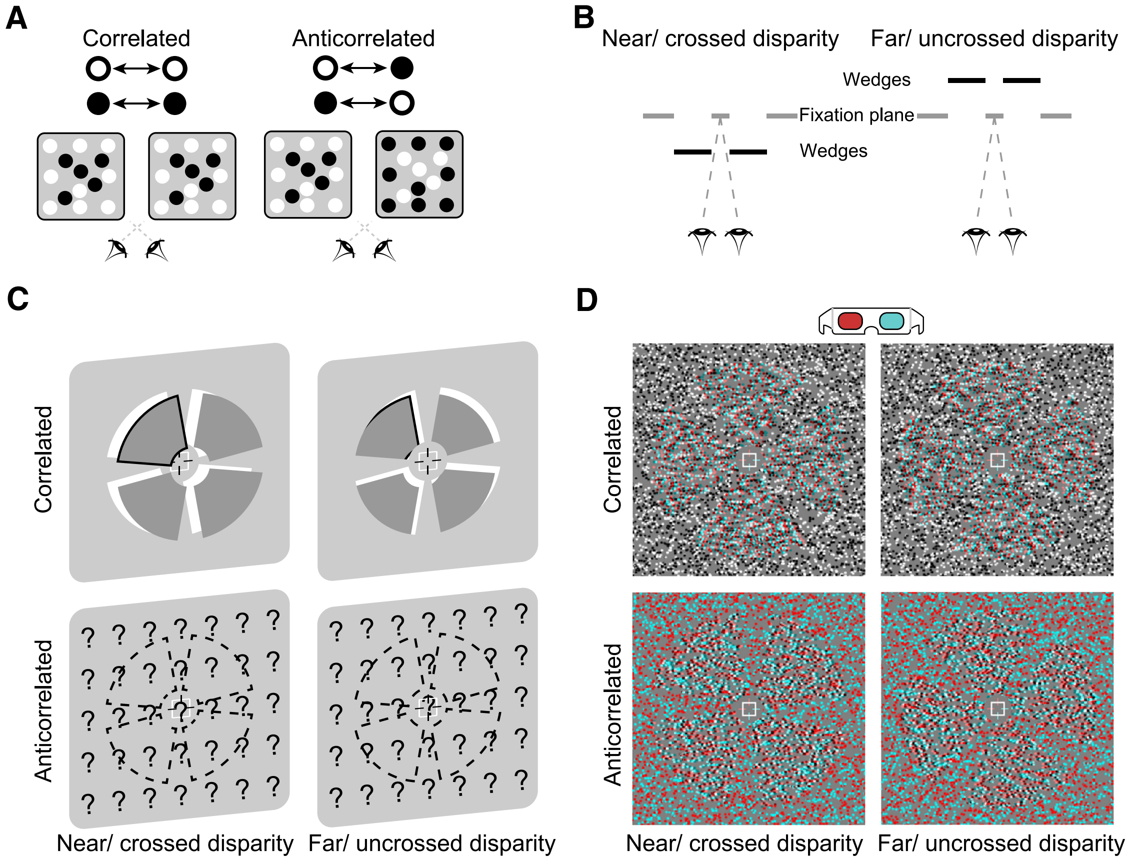

Figure 2. Schematic illustration of the stimuli and experimental conditions. ***A***, A simplified schematic representation of RDSs. Correlated RDS stimuli were created by showing dots indicating the stimulus presented at the same contrast in both eyes (e.g., a black dot in the left eye matched a black dot in the right eye). The same disparity configurations were rendered in the anticorrelated RDS, where the contrasts of dots in the two eyes were reversed (e.g., a white dot in one eye matched a black dot in the other). This anticorrelated stimulus does not evoke a reliable disparity-defined impression of 3D structure (stereoscopic perception). ***B***, A schematic representation of the disparity-defined 3D structure of the stimuli. The gray lines represent the fixation plane of the display screen where observers were instructed to fixate their eyes (zero disparity). One of two perceived depth configurations was presented on each trial; left, the diagram shows the crossed disparity configurations in which the wedges (represented by black lines) were closer to the observer than the fixation plane (i.e., disparity near), right, the diagram shows the uncrossed disparity in which the wedges were farther from the observer than the fixation plane (i.e., disparity far). The magnitude of the disparity was the same (i.e., disparity near = −disparity far). ***C***, Diagram of the perceived depth arrangement in the stimuli. Four disparity-defined wedges were simultaneously presented at near or far disparity. For the correlated stimuli, participants perceived the wedge structure. Note: The black outline on the wedges is for illustrative purposes only. For the anticorrelated stimuli, the position of the wedges is indicated by dashed outlines; however, participants could not perceive the wedge structure. ***D***, Example stimuli used in the experiment, designed for red-cyan anaglyph viewing. Vernier task stimuli were presented on the center of the stimulus as shown by the lines of the cross hair.

fixation plane. The four wedges were simultaneously rendered with the same binocular correlation form and disparity. Further, a static grid with squares surrounded the RDS (not shown in Fig. 2), providing an unambiguous reference and enabled stable vergence during fixation.

To avoid confusion between the perception of the 3D structure (i.e., depth perception) and different sampling positions relative to the cortical surface (i.e., cortical depth), in this article we use the term "depth" to refer to neuroanatomical positions. We refer to the perception of a 3D structure as 3D/stereoscopic perception.

Experiments were controlled using MATLAB (MathWorks) and Psychophysics Toolbox version 3.0 (Brainard, 1997; Pelli, 1997). Stimuli were presented using a projector and a mirror setup (1920 × 1080 pixels resolution, 60 Hz frame rate) at a viewing distance of 99 cm. Participants viewed red and cyan anaglyphs through color-filter glasses.

Experimental design and statistical analysis

fMRI design. A 2 × 2 block experimental design was used with the factors Stereo (correlated vs anticorrelated RDS) and Disparity (near vs far). The fMRI experiment comprised a maximum of six runs. Three participants completed six runs, one participant completed five runs, two participants completed four runs, and one participant completed two scans of six runs and four runs on 2 separate days. The amount of time available to collect experimental data depended on the initial setup time for each participant (e.g., testing visibility of the RDS stimuli in the scanner and MRI-related calibrations like shimming).

Each run lasted 8 min 24 s, starting with a fixation block (12 s), followed by 40 stimulus blocks, 10 blocks for each of the four conditions, and ended with a fixation block (12 s). The order of the blocks was counterbalanced within and across runs and participants. Each block lasted 12 s and comprised 10 stimuli of the same condition. Each stimulus was displayed for 900 ms followed by a 300 ms interstimulus interval, with a randomized jitter of disparity (±0.5 arcmin).

During scanning, participants engaged in an attentionally demanding dichoptic Vernier detection task at the fixation marker (Popple et al., 1998; Murphy et al., 2013). Briefly, participants were instructed to fixate a central crosshair fixation marker that was present throughout experimental scans. Two of the lines of the crosshair were presented to one of the eyes (e.g., top and left lines in the left eye) and the other two to the other eye (e.g., bottom and right lines in the right eye; Fig. 2*D*). Participants were instructed to alter their horizontal and/or vertical eye vergence so that the crosshairs were properly aligned to form a cross. In addition, a small additional Vernier target was briefly flashed (900 ms) in one eye, and the participants were asked to indicate its position (left vs right under a two-alternative forced-choice paradigm) relative to the top line of the fixation marker.

To localize the visual areas, a region of interest (ROI) localizer scan was also acquired. A circular checkerboard of the size of the RDS stimuli

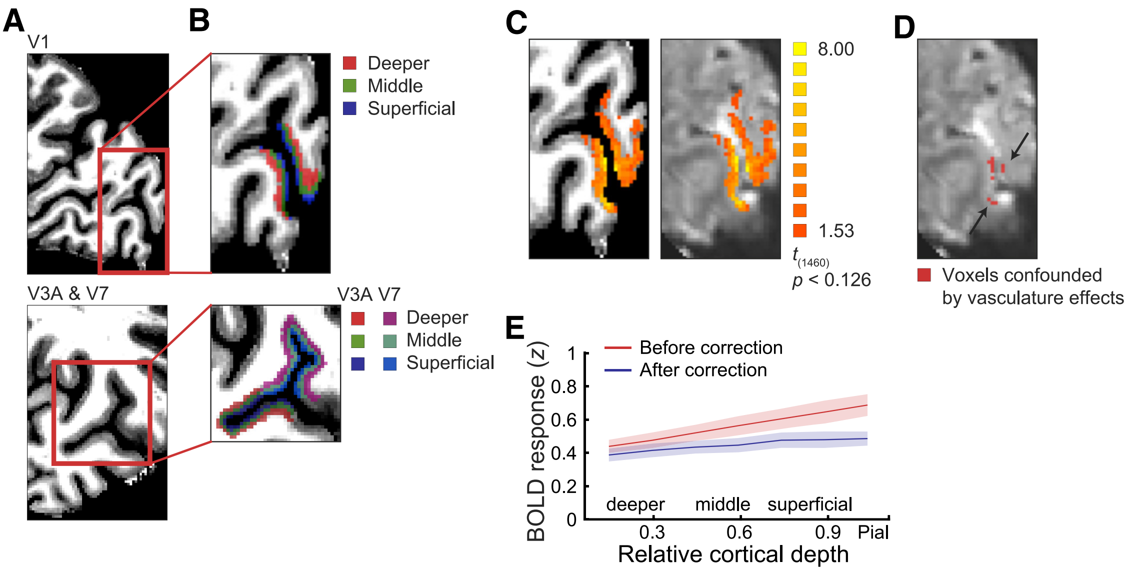

Figure 3. fMRI layer definition and vascular correction. ***A***, Sagittal (top) and transverse (bottom) view of the anatomic image of a sample participant. Red inserts indicate ROIs in visual cortex. ***B***, Layers definition map overlaid on an anatomic image (top, V1, red, deeper layers; green, middle layers; blue, superficial layers; bottom, V3A, red, deeper layers; green, middle layers; blue, superficial layers; V7, purple, deeper layers; light green, middle layers; light blue, superficial layers). V7 definition followed the Wang et al. (2015) atlas and was validated against the atlas derived from the Human Connectome Project (HCP) data (Benson et al., 2018) showing 83% overlap in ROI definition. MVPA showed similar results across atlases used for ROI definition [significant cortical depth (deeper, middle, superficial layers) × condition (correlated, anticorrelated RDS)] interaction for MVPA accuracy in V7 using the Wang et al. atlas ($F_{(2,12)} = 4.37$, $p = 0.037$) or the HCP atlas ($F_{(2,12)} = 4.74$, $p = 0.030$). ***C***, BOLD activation map (stimulus vs fixation) overlaid on the anatomic (left) and functional data (right) in V1. ***D***, Voxels confounded by vasculature-related effects (red, highlighted by arrows) overlaid on mean functional image in V1. ***E***, Mean normalized BOLD in V3A before (red) and after (blue) correction for vasculature-related effects across cortical depth, showing reduced superficial bias after correction. Similar results were observed for V1 and V7. The stronger BOLD decrease in upper (i.e., superficial, middle) rather than deeper layers after correction suggests that our approach for correcting vasculature-related effects controlled substantially for the superficial bias. Shaded areas indicate SEM across participants.

was presented flickering at 8 Hz. The localizer scan lasted 5 min 36 s and started with a 16 s fixation, followed by 20 stimuli. Each stimulus was displayed for 2 s with a 14 s interstimulus interval. In the same scanning session, anatomic data and fMRI data for retinotopic mapping were collected following standard procedures (Engel et al., 1997).

MRI data acquisition. Imaging data were acquired on a 7T Magnetom scanner (Siemens) at the Scannexus Imaging Centre, Maastricht, The Netherlands. We used a 32-channel phased-array head coil (NOVA Medical), and a 2D gradient echo-echo planar imaging (GE-EPI) sequence [Moeller et al., 2010; repetition time (TR) = 2 s, echo time (TE) = 25 ms, voxel size = 0.8 mm isotropic, field of view (FOV) = 148 × 148 mm^2, number of slices = 56, partial Fourier = 6/8, GRAPPA factor = 3, multiband factor = 2, bandwidth = 1168 Hz/pixel, echo spacing = 1 ms, flip angle = 70°]. The FOV covered occipitotemporal and posterior parietal areas; manual shimming was performed before the acquisition of the functional scans. Anatomical images were acquired using MP2RAGE T1-weighted sequence (TR = 5 s, TE = 2.51 ms, voxel size = 0.65 mm isotropic, FOV = 208 × 208 mm^2, 240 sagittal slices).

MRI data analysis

Anatomical data analyses. T1-weighted anatomic data were used for coregistration and 3D cortex reconstruction. Gray- and white-matter segmentation (Fig. 3*A*) was obtained on the MP2RAGE images using FreeSurfer (https://surfer.nmr.mgh.harvard.edu; Fischl, 2012) and manually improved for the ROIs (i.e., V1, V3A, V7) using ITK-SNAP (http://www.itksnap.org/; Yushkevich et al., 2006). The refined segmentation was used to obtain a measurement of cortical thickness. Following previous studies, we assigned voxels to three cortical depths (deeper, middle, superficial layers; Fig. 3*B*) using the equivolume approach (Waehnert et al., 2014; Kemper et al., 2018) as implemented in BrainVoyager (version 20.6; Brain Innovation). This approach has been shown to reduce misclassification of voxels to layers, in particular for ROIs presenting high curvature. Information from the cortical thickness map and gradient curvature was used to generate four grids at different cortical depths (ranging from 0 white matter to 1 gray matter). Mapping of each voxel to a layer was obtained by computing the Euclidean distance of each gray-matter voxel to the grids: the two closest grids represent the borders of the layer to which a voxel is assigned (Fig. 3*C*). Note that because of limitations in the UHF imaging resolution, these MRI-defined layers indicate distance (i.e., cortical depth) from the gray matter/white matter and the gray matter/cerebrospinal fluid boundaries rather than one-to-one mapping to the cytoarchitectonically defined layers of the human neocortex.

fMRI data analyses. The functional data were analyzed using BrainVoyager and custom MATLAB code. The first volume at the beginning of each run was discarded to ensure that longitudinal magnetization reached steady state. Preprocessing of the functional data involved three steps, starting with correction of distortions because of a nonzero off-resonance field; that is, at the beginning of each functional run, five volumes with an inverted phase encoding direction were acquired and used to estimate a voxel displacement map, which was subsequently applied to the functional data using Correction Based on Opposite Phase Encoding (BrainVoyager, Brain Innovation). The distortion-corrected data underwent slice-timing correction, head motion correction (the single band image acquired at the beginning of each run was used as reference in the alignment), high-pass temporal filtering (using a GLM with Fourier basis set at two cycles), and removal of linear trends. To validate the alignment, we calculated the mean EPI image of each functional run for each ROI and estimated the spatial correlation between these mean EPI images. We performed a manual adjustment of the alignment if the spatial correlation was below 0.85 (Marquardt et al., 2018). Preprocessed functional data were coaligned to the anatomic data using the boundary-based registration approach, as implemented in BrainVoyager (Greve and Fischl, 2009). Results were manually inspected and further adjusted where needed.

ROIs definition. We used the data from the retinotopic mapping scan to identify visual areas V1 and V3A based on standard phase-encoding methods. Participants viewed rotating wedges that created traveling waves of neural activity (Sereno et al., 1995; Engel et al., 1997). Area V7 was defined at the posterior intraparietal sulcus for each participant based on anatomic templates following Wang et al. (2015) and provided by Benson et al. (2012, 2014; https://hub.docker.com/r/nben/occipital_atlas/). This procedure uses the individual participant-based segmentation obtained with FreeSurfer and an anatomic probabilistic template to estimate the best location for the ROI (i.e., V7). Our definition of V7 was consistent with the atlas derived from Human Connectome Project (Benson et al., 2018). We found an 83% overlap in the definition of V7 between atlases, and the results showed similar patterns when comparing across ROI definitions. Each area was subsequently inspected to ensure consistent definition across participants; that is, we checked whether the ROI (1) was located at the correct anatomic location and (2) covered only gray matter rather than white matter or CSF.

For each ROI and participant, we modeled BOLD signals using a GLM with four regressors, one per stimulus condition (Stereo × Disparity), and included the estimated head motion parameters as nuisance regressors. Similarly, we modeled the localizer BOLD signals using a GLM with one stimulus regressor, fixation, and motion parameters as nuisance regressors. The resulting t statistical map was thresholded (main scan, $t = 1.53$, $p = 0.125$; localizer scan, $t = 1.96$, $p = 0.05$) to select voxels within each ROI that showed stronger responses to the stimulus conditions compared with the fixation baseline (Fig. 3*C*).

Correcting for vasculature-related effects. Voxel selection within each ROI was further refined by excluding voxels that were confounded by vasculature effects, which are known to contribute to a superficial bias in the measured BOLD signal; that is, increased BOLD with increasing distance from white matter. In particular, it has been shown that the BOLD signal measured using GE-EPI (i.e., T2*-weighted) is confounded by macro- and micro-vasculature signals (Uğurbil et al., 2003; Yacoub et al., 2005; Uludağ et al., 2009). The macro-vasculature contribution is because of veins penetrating the gray matter and running through its thickness, as well as large pial veins situated along the surface of the gray matter (Duvernoy et al., 1981). This results in increased sensitivity (i.e., strong BOLD effect) but decreased spatial specificity of the measured signal. The latter can be understood by the mechanics of the draining veins carrying deoxygenated hemoglobin downstream from the true neuronal site of neural activation, leading to a response spatially biased toward the pial surface, an effect known as superficial bias.

Here, we took the following approach to reduce superficial bias because of vasculature contributions (Jia et al., 2020; Zamboni et al., 2020). First, following previous work (Olman et al., 2007), we computed the temporal signal-to-noise ratio (tSNR) for each voxel in each ROI (V1, V3A, V7). We used tSNR to identify voxels near large veins that are expected to have large variance and a low-intensity signal because of the local concentration of deoxygenated hemoglobin, resulting in a short T2* decay time (i.e., dark intensity in a T2*-weighted image). We identified voxels with low tSNR (lower than 2 SD; mean tSNR across V1 smaller than 13.26 ± 1.02, V3A smaller than 14.46 ± 1.31, V7 smaller than 13.99 ± 1.75) and checked the correspondence with voxels of lower intensities on the T2*-weighted images. Second, it has been shown that high t values on an fMRI statistical map are likely to arise from large pial veins (Polimeni et al., 2010; Kashyap et al., 2018). Therefore, voxels with low tSNR values or t score values above the 90th percentile (mean t score across V1 larger than 6.24 ± 1.76, V3A larger than 3.84 ± 1.00, V7 larger than 3.11 ± 0.48) of the t score distribution obtained by the GLM described above were removed from further analysis. We used these two approaches to correct the BOLD signal from confounding vasculature effects.

Further, to account for possible differences in signal strength across cortical layers because of thermal and physiological noise as well as signal gain (Goense et al., 2012; Havlicek and Uludağ, 2020), we (1) matched the number of voxels across layers per participant and ROI and (2) z-scored the time courses within cortical layers per ROI, controlling for differences in signal levels across layers while preserving signal differences across conditions (after correction of vascular contributions; Lawrence et al., 2019a). To validate this approach, we compared the mean normalized fMRI responses before and after correction. For each participant and run, we extracted the mean normalized fMRI responses per block. To account for hemodynamic delay in our blocked design, we shifted the time course by two TRs (i.e., 4 s) from the onset of the block. Further, to capture the BOLD signal from the last stimulus presentation per block, we included signals from one TR after the end of each block. That is, we included fMRI responses between the third and seventh TR (i.e., 4–14 s) after stimulus onset. The normalized fMRI responses were averaged across time points, stimulus presentation, and runs. Repeated-measures ANOVA was used to test the BOLD signal (before vs after correction) and cortical depths (deeper, middle, superficial layers; see below, Control analyses).

Multivariate pattern analysis. Following our previous work (Preston et al., 2008; Jia et al., 2020), we used MVPA to discriminate BOLD responses related to near versus far disparity stimuli across cortical layers in the visual cortex. For each ROI and participant, we calculated per voxel a t score statistic by comparing activity for stimuli versus fixation. We used this statistic to rank the voxels within cortical depths (deeper, middle, superficial layers) per ROI and selected 175 voxels per layer with the higher t score to include in the MVPA, as MVPA accuracy saturated across all participants for these voxel pattern sizes in the corresponding regions. This voxel selection procedure ensured that comparisons of MVPA accuracy could not be confounded by a varying number of voxels across participants. We then extracted mean normalized fMRI responses between the third and seventh TR (i.e., 4–14 s) after block onset for this pattern of voxels per ROI and participant. We trained a linear classifier using the Library for Support Vector Machines with the default C value ($C = 1$; https://www.csie.ntu.edu.tw/~cjlin/libsvm/; Chang and Lin, 2011) implemented in MATLAB to discriminate the near from the far disparity stimulus. We computed MVPA accuracy using a leave-one-run-out cross-validation. That is, we divided the data set into training (60–180 patterns depending on the number of scanning runs per participant) and test (20 patterns) data. We averaged the MVPA accuracy across folds. We used repeated-measures ANOVAs to assess differences in MVPA accuracy across conditions (correlated, anticorrelated RDS), cortical depths (deeper, middle, superficial layers), and ROIs (V1, V3A, V7). Mauchly's W tests were used to determine whether the assumption of sphericity was violated. If necessary, we corrected the degrees of freedom by the Greenhouse–Geisser correction (for $\varepsilon < 0.75$). *Post hoc* comparisons were conducted using pairwise t test comparisons. Within-subject SEM was adjusted using the Cousineau–Morey method (O'Brien and Cousineau, 2014).

To corroborate the MVPA results, we conducted a cross-validated linear discriminant contrast (LDC) analysis (Diedrichsen et al., 2016; Walther et al., 2016). The linear discriminant contrast is centered on zero under the null hypothesis of no reliable differences between the near versus far conditions. We used the same data and voxels as in the MVPA. We divided the dataset into training and test data and performed a leave-one-run-out cross-validation. For each cross-validation, we contrasted signals from the near against the far stimulus blocks to generate the representation distance metric for both the training and test datasets. The distance matrix from the training datasets was normalized using the sparse covariance matrix of the noise residuals to produce the weights vector. The LDC is the dot product of the representation distance metric for the test dataset and the weight matrix estimated from the training dataset. Finally, we averaged the LDC values across cross-validations per participant.

Informational connectivity analysis. We used informational connectivity to identify layers that share synchronized discriminability of activity related to stimulus-specific multivoxel pattern information (Coutanche and Thompson-Schill, 2014; Anzellotti and Coutanche, 2018; Koster et al., 2018; Jia et al., 2020). We examined intercortical informational connectivity based on shared changes (fluctuations) in pattern discriminability over time as this approach has been shown to be more sensitive than univariate functional connectivity. To track the flow of multivariate information across time (i.e., across blocks), we measured the fluctuations (covariance) in MVPA discriminability by calculating distance information from the classification hyperplane. In particular, we selected 175 voxels with the higher t score and used the same multivoxel near versus far disparity patterns as in the MVPA. For each ROI and layer, we extracted distance information for the test data per block from the trained classifiers. We calculated layer-specific connectivity by Spearman's correlation between the foldwise distance of different layers. We transformed the correlation coefficients using Fisher's z transform and conducted repeated-measures ANOVAs to compare across conditions (correlated, anticorrelated RDS) and ROI pairs (V1–V3A, V3A–V7, V1–V7) per pathway (feedforward, feedback). Note that both feedforward and feedback processing involve interactions between superficial layers of lower visual areas and deeper layers of higher visual areas; that is, we cannot differentiate feedforward from feedback processing based on superficial-to-deeper-layer connectivity. Thus, we focused our investigations on the connectivity between deeper layers that is known to be related to feedback processing (Rockland and Pandya, 1979; Maunsell and van Essen, 1983).

Data availability

Data files are available at the Cambridge Data Repository: https://doi.org/10.17863/CAM.74947.

Results

Disparity representations across cortical depths

We tested fMRI responses across cortical depths in the visual cortex when participants were presented with disparity-defined stimuli. We rendered binocular disparities in RDSs in which the 3D structure of the stimulus is only apparent once binocular correspondence has been established. Correlated RDS stimuli (Fig. 2*A*) support a clear interpretation of stereoscopic structure; however, the same disparity information can be rendered in anticorrelated RDS stimuli (aRDS, Fig. 2*A*), which do not give rise to a clear perceptual interpretation of depth.

These stimuli are informative because although dense aRDS do not support a perceptual interpretation of 3D structures, the disparities they contain are registered by neurons in the primary visual cortex (Cumming and Parker, 1997) but not at higher levels of the visual system (Janssen et al., 2003). Anticorrelated stimuli have therefore been interpreted as false matches that should be vetoed to solve the stereo correspondence problem (Scharstein and Szeliski, 2002) and produce a close similarity between neural responses and the perceptual interpretation of a 3D structure. Thus, contrasting fMRI signals for correlated versus anticorrelated stimuli provides a useful means to test neural representations that relate to stereoscopic perception. We rendered all stimuli (correlated, anticorrelated) to contain either crossed or uncrossed binocular disparities (nearer or farther from the fixation point; Fig. 2*B*). We compared fMRI responses for these stimuli (crossed vs uncrossed) across cortical depths in areas V3A and V7, which are known to be engaged by correlated RDS stimuli (Preston et al., 2008; Goncalves et al., 2015), versus V1, which is known to respond to both correlated and anticorrelated stimuli (Bridge and Parker, 2007; Preston et al., 2008; Ip et al., 2014).

For each participant, we segmented the visual areas and assigned voxels to three cortical depths (deeper, middle, superficial layers) using an equivolume approach (see above, MRI data analysis, Anatomical data analyses; Fig. 3*A*, *B*). Voxels identified as containing large veins were removed from the analysis to improve the spatial specificity of the cortical depth profiles (Fig. 3*C*, *D*). We used MVPA to discern disparity-specific (i.e., near vs far disparities) fMRI signals when participants were presented with correlated versus anticorrelated RDS stimuli. In particular, we tested whether linear classifiers that were trained on fMRI signals from multivoxel patterns across cortical depths (deeper, middle, superficial) in V1, V3A, and V7 discriminated between near versus far disparity stimuli based on differences in crossed versus uncrossed disparity signals. We hypothesized that higher MVPA accuracy for correlated compared with anticorrelated RDS stimuli would indicate disparity-specific representations related to stereoscopic perception.

A three-way repeated-measures ANOVA (condition: correlated, anticorrelated RDS; cortical depth: deeper, middle, superficial layers; ROI: V1, V3A, V7) showed significant main effects of condition (correlated, anticorrelated RDS; $F_{(1,6)} = 30.42$, $p = 0.001$; Fig. 4*A*) and cortical depth (deeper, middle, superficial layers; $F_{(2,12)} = 4.286$, $p = 0.039$), but no significant main effect of ROI (V1, V3A, V7; $F_{(1.2,7.4)} = 3.60$, $p = 0.093$). We observed a significant condition × cortical depth interaction ($F_{(2,12)} = 8.65$, $p = 0.005$) and a significant condition × ROI interaction ($F_{(2,12)} = 7.08$, $p = 0.009$) but no significant three-way interaction ($F_{(4,24)} = 1.15$, $p = 0.358$).

Further, a two-way repeated-measures ANOVA (condition × cortical depth) in V3A showed a significantly higher MVPA accuracy for upper (i.e., superficial, middle) than deeper layers (main effect of cortical depth: $F_{(2,12)} = 7.01$, $p = 0.010$), for correlated than anticorrelated stimuli (main effect of condition: $F_{(1,6)} = 38.03$, $p = 0.001$), and a significant condition × cortical depth interaction ($F_{(2,12)} = 6.02$, $p = 0.015$), suggesting layer-specific disparity processing in V3A. *Post hoc* comparisons showed that MVPA accuracy for correlated stimuli was significantly higher in superficial ($t_{(6)} = 3.13$, $p = 0.020$) and middle ($t_{(6)} = 2.45$, $p = 0.049$) than deeper layers. There were no significant differences between superficial and middle layers for correlated stimuli ($t_{(6)} = 2.26$, $p = 0.065$).

Similarly, for V7 a two-way repeated-measures ANOVA (condition × cortical depth) showed significantly higher MVPA accuracy for upper than deeper layers (main effect of cortical depth: $F_{(2,12)} = 4.37$, $p = 0.037$), for correlated than anticorrelated stimuli (main effect of condition: $F_{(1,6)} = 31.46$, $p = 0.001$), and a significant condition × cortical depth interaction ($F_{(2,12)} = 4.97$, $p = 0.027$), suggesting layer-specific disparity processing in V7. *Post hoc* comparisons showed that MVPA accuracy for correlated stimuli was higher in superficial ($t_{(6)} = 3.85$, $p = 0.008$) and middle ($t_{(6)} = 2.62$, $p = 0.040$) than deeper layers. There were no significant differences between superficial and middle layers for correlated stimuli ($t_{(6)} = 0.33$, $p = 0.751$).

In contrast to the MVPA results in V3A and V7, in V1 a two-way repeated-measures ANOVA (condition × cortical depth) showed significantly higher MVPA accuracy for correlated than anticorrelated stimuli (main effect of condition: $F_{(1,6)} = 10.24$, $p = 0.019$) but no significant main effect of cortical depth ($F_{(2,12)} = 0.90$, $p = 0.431$) nor condition × cortical depth interaction ($F_{(1.1,6.3)} = 1.41$, $p = 0.280$).

Finally, a cross-validated LDC analysis corroborated our results on MVPA accuracy (Diedrichsen et al., 2016; Walther et al., 2016). A three-way repeated-measures ANOVA showed a significant three-way interaction (condition × cortical depth × ROI, $F_{(4,24)} = 6.35$, $p = 0.001$; Fig. 4*B*). Further, two-way repeated-measures ANOVAs on the LDC distance per ROI showed a significant two-way interaction (condition × cortical depth) in V3A ($F_{(1.1,6.9)} = 15.21$, $p = 0.005$) and V7 ($F_{(2,12)} = 12.06$, $p = 0.001$), but not in V1 ($F_{(2,12)} = 2.92$, $p = 0.092$). *Post hoc* comparisons in V3A showed higher LDC distance for correlated stimuli in superficial than deeper ($t_{(6)} = 4.16$, $p = 0.018$) and middle ($t_{(6)} = 4.85$, $p = 0.009$) layers but not middle versus deeper layers ($t_{(6)} = 3.21$, $p = 0.055$). *Post hoc* comparisons in V7 showed higher LDC distance for correlated stimuli in superficial versus deeper layers ($t_{(6)} = 4.78$, $p = 0.009$) but not superficial versus middle layers ($t_{(6)} = 2.67$, $p = 0.111$) or middle versus deeper layers ($t_{(6)} = 2.96$, $p = 0.076$).

Together our results suggest that disparity representations for stereoscopic perception (i.e., higher classification accuracy for correlated than for anticorrelated stimuli) in V3A and V7 are

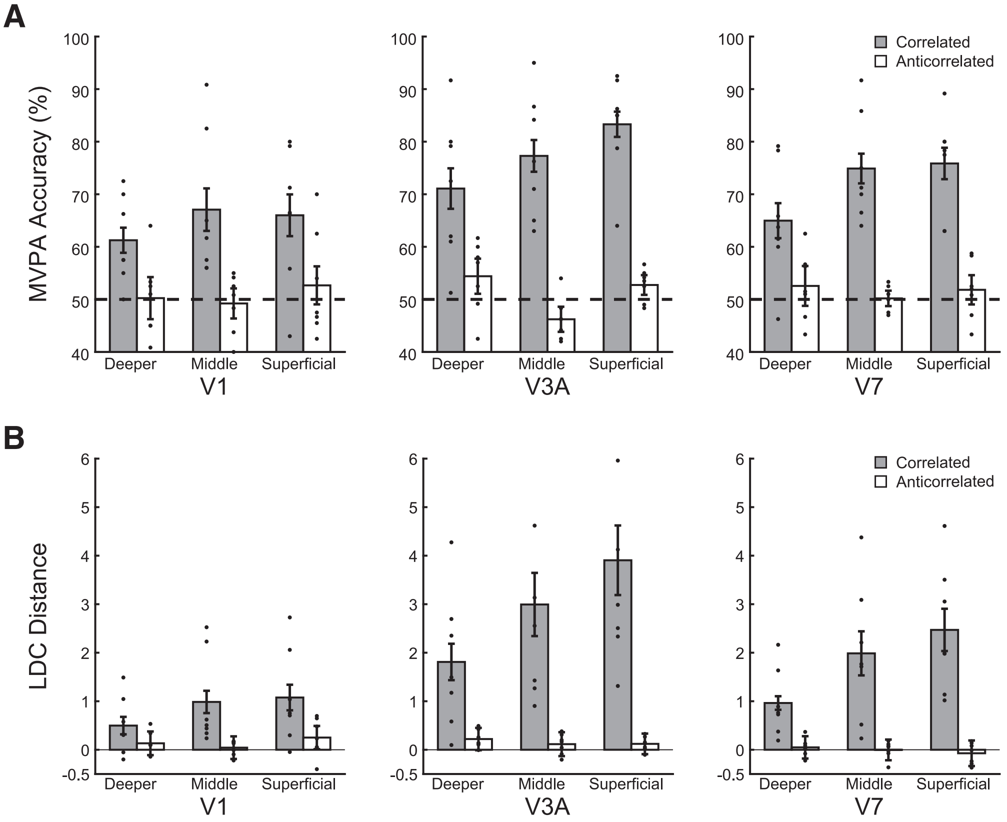

Figure 4. Pattern classification analyses across cortical depth. ***A***, MVPA accuracy across V1, V3A, and V7 layers for correlated (gray bar) and anticorrelated (white bar) stimuli in the near versus far disparity classification. Dotted line indicates MVPA accuracy at 50% chance. ***B***, Linear discriminant contrast distance across V1, V3A, and V7 layers for correlated (gray bar) and anticorrelated (white bar) stimuli in the near versus far disparity contrast. Error bars indicate within-subject SEM across participants. Filled dots indicate individual data.

layer specific. Despite the lack of a significant three-way interaction on MVPA accuracy (condition × cortical depth × ROI), potentially because of the small sample size, the LDC distance analysis showed a significant condition × cortical depth × ROI interaction. This analysis suggests disparity representations for stereoscopic perception in V3A and V7 that are specific to upper rather than deeper cortical layers. Finally, the differences in MVPA accuracy between correlated and anticorrelated stimuli could not be simply because of differences in attention as participants performed an attentionally demanding task on the fixation point during scanning. Further, our stimuli were designed to reduce differences in vergence eye movements across conditions. In particular, (1) a stable, low-spatial frequency pattern in the plane of the screen surrounded the stimuli and (2) participants were instructed to use the horizontal and vertical nonius lines to assist them in ensuring correct eye alignment at all times.

Control analyses

To validate our results and control for potential confounds we conducted the following additional analyses.

First, it has been shown that the overall BOLD signal as measured by GE-EPI is higher at the cortical surface because of vascular contributions (Uğurbil et al., 2003; Yacoub et al., 2005; Uludağ et al., 2009) resulting in loss of spatial specificity (Kay et al., 2019). Following our previous work (Jia et al., 2020; Zamboni et al., 2020), we combined several approaches to reduce this superficial bias by removing voxels with low temporal signal-to-noise ratio and high *t* statistic for stimulation contrast (see above, Correcting for vasculature-related effects). We then *z*-scored each voxel's time course to account for possible differences in signal strength and variance because of thermal or physiological noise across layers while preserving differences among conditions (Lawrence et al., 2019a). Figure 3*E* shows that following these corrections the superficial bias was significantly reduced in V3A. That is, the magnitude of BOLD signals from voxels closer to the pial surface was reduced, as indicated by a significant interaction between the BOLD signal from different cortical depths (deeper, middle, superficial layers) before versus after correction ($F_{(2,12)} = 28.61$, $p < 0.001$). That is, the superficial bias corrections resulted in decreased BOLD signals in upper layers as indicated by *post hoc* comparisons (middle layers: $t_{(6)} = 6.95$, $p < 0.001$; superficial layers: $t_{(6)} = 7.56$, $p < 0.001$). A similar reduction in superficial bias was observed in V1 ($F_{(1.1,6.6)} = 18.89$, $p = 0.003$; *post hoc* comparisons: middle layers: $t_{(6)} = 12.57$, $p < 0.001$; superficial layers: $t_{(6)} = 12.07$, $p < 0.001$) and V7 ($F_{(1.1,6.3)} = 16.25$, $p = 0.006$; *post hoc* comparisons: middle layers: $t_{(6)} = 5.24$, $p = 0.002$; superficial layers: $t_{(6)} = 4.88$, $p = 0.003$). Thus, it is unlikely that our MVPA results after vasculature correction were significantly confounded by the superficial bias.

Second, we applied a spatial regression approach (Kok et al., 2016; Markuerkiaga et al., 2016; Koster et al., 2018) to control for signal contribution from draining veins. In particular, intracortical veins running perpendicular to the cortical surface are known to drain blood from deeper layers of the cortex to larger pial veins situated along the gray-matter surface, resulting in loss of spatial specificity and intralayer BOLD signal contamination. To unmix the signal from adjacent layers, for each voxel in the superficial layers, we found its nearest neighbors in the middle layers. We then averaged the time course of these voxels and

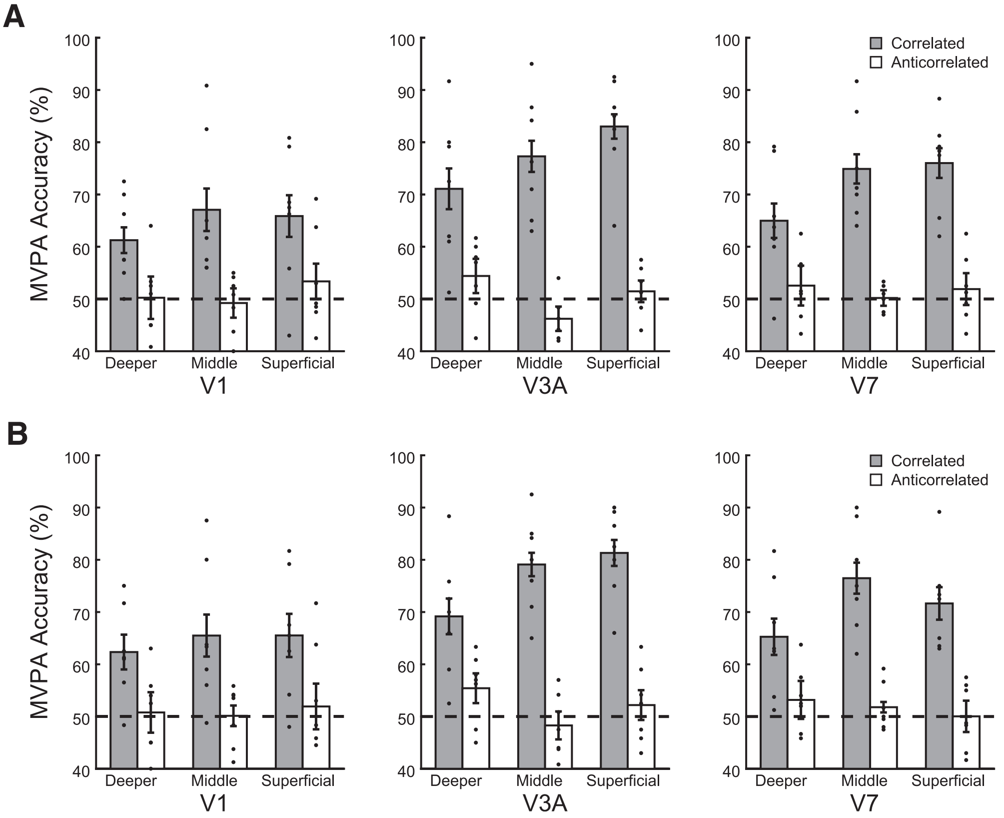

Figure 5. Control analyses. ***A***, MVPA accuracy for correlated (gray bar) and anticorrelated (white bar) stimuli in the near versus far disparity classification in V1, V3A, and V7 layers after regressing out the signal from the adjacent voxels in middle layers. ***B***, MVPA accuracy for correlated (gray bar) and anticorrelated (white bar) stimuli in the near versus far disparity classification in V1, V3A, and V7 layers after regressing out mean voxel response per condition (i.e., univariate information). Dotted line indicates MVPA accuracy at 50% chance. Error bars indicate within-subject SEM across participants. Filled dots indicate individual data.

regressed the mean time course of each voxel in the superficial layers. MVPA following this correction showed a significant condition × cortical depth interaction in V3A ($F_{(2,12)} = 7.27$, $p = 0.009$, Fig. 5*A*) and V7 ($F_{(2,12)} = 4.73$, $p = 0.031$). Further, we observed higher MVPA accuracy for correlated stimuli in superficial ($t_{(6)} = 2.45$, $p = 0.049$) and middle ($t_{(6)} = 2.91$, $p = 0.027$) than deeper V3A layers but not superficial versus middle layers ($t_{(6)} = 2.30$, $p = 0.061$) and higher MVPA accuracy for correlated stimuli in superficial ($t_{(6)} = 3.85$, $p = 0.008$) and middle ($t_{(6)} = 2.68$, $p = 0.037$) than deeper V7 layers but not superficial versus middle layers ($t_{(6)} = 0.39$, $p = 0.713$), consistent with stronger stereoscopic processing in upper than deeper V3A and V7 layers. That is, our results remained significant after these corrections, suggesting that our results are unlikely to be significantly confounded by vasculature-related artifacts.

Third, to ensure that our classification approach was not overpowered and did not suffer from any bias, we ran the classification with the data labels shuffled. Theoretically, this should result in classification accuracies at chance. The results for the classification of 5000 permutations of shuffled data for the near versus far classification did not differ significantly from chance (all ps > 0.500, false discovery rate corrected), suggesting that the MVPA extracted reliable voxel pattern information.

Fourth, to ensure that differences in univariate BOLD signals across ROIs and cortical depths did not account for our MVPA results, we trained the classifier after regressing out the mean normalized response across voxels for each ROI and condition. This analysis showed similar results (Fig. 5*B*) to the main MVPA (Fig. 4*A*). Two-way repeated-measures ANOVAs showed significant condition × cortical depth interaction in V3A ($F_{(2,12)} = 9.87$, $p = 0.003$) and V7 ($F_{(2,12)} = 4.82$, $p = 0.029$), but not in V1 ($F_{(1.1,6.4)} = 0.30$, $p = 0.617$), suggesting that our MVPA results relate to multivoxel pattern representations of 3D structures rather than an overall BOLD signal in each ROI.

Fifth, to ensure that our results were not specific to voxel number ($n = 175$) selected for MVPA, we tested the MVPA with different voxel pattern sizes (i.e., 200, 225, and 250 voxels). MVPA using these voxel patterns showed similar results. In particular, for 200 voxels, two-way repeated-measures ANOVAs showed significant condition × cortical depth interaction in V3A ($F_{(1.1,6.5)} = 6.46$, $p = 0.039$) and V7 ($F_{(2,12)} = 7.19$, $p = 0.009$) but not in V1 ($F_{(2,12)} = 0.18$, $p = 0.841$). For 225 voxels, two-way repeated-measures ANOVAs showed significant condition × cortical depth interaction in V3A ($F_{(2,12)} = 4.00$, $p = 0.047$) and V7 ($F_{(2,12)} = 7.48$, $p = 0.008$) but not in V1 ($F_{(2,12)} = 0.28$, $p = 0.762$). For 250 voxels, two-way repeated-measures ANOVAs showed significant condition × cortical depth interaction in V3A ($F_{(2,12)} = 4.12$, $p = 0.043$) and V7 ($F_{(2,12)} = 5.17$, $p = 0.024$) but not in V1 ($F_{(2,12)} = 0.31$, $p = 0.738$). These results are consistent with our main MVPA results using 175 voxels, suggesting that our results are unlikely to be significantly affected by choice of pattern size.

Informational connectivity analysis

UHF fMRI allows us to interrogate the finer functional connectivity across brain areas based on known anatomic models of connectivity across cortical layers. Here, we tested functional connectivity across visual areas (V1, V3A, V7) to investigate the

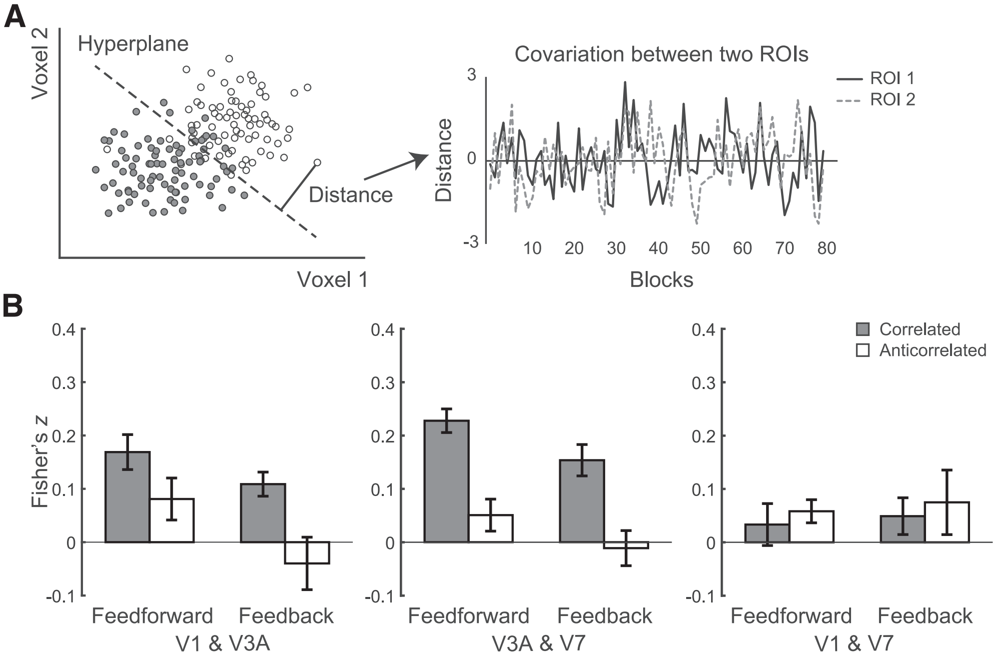

Figure 6. Informational connectivity analysis. ***A***, Schematic illustration of the procedure followed for the MVPA-based functional connectivity analysis. For each ROI and block, we calculated the distance to the classifier hyperplane (indicated by the dotted line) as an index of pattern discriminability (left). Filled and open dots indicate test patterns from different classes (i.e., near vs far disparity). For each ROI, we calculated a time series of distances across blocks during each scanning session. Spearman's correlation was used to calculate covariance between time series across ROIs (right). ***B***, Functional connectivity (Fisher's *z*) between V1 and V3A, V3A and V7, and V1 and V7: feedforward connectivity between superficial layers of earlier visual areas to middle layers of higher areas, feedback connectivity between deeper layers across visual areas for correlated (gray bar) and anticorrelated (white bar) stimuli. Error bars indicate within-subject SEM across participants.

role of feedforward and feedback processing for stereoscopic perception. Although UHF imaging resolution does not support one-to-one mapping between MRI-defined cortical depths and cytoarchitectonically defined layers, previous UHF imaging studies (Kok et al., 2016; Huber et al., 2017; Sharoh et al., 2019; Moerel et al., 2020) have provided a framework of feedback and feedforward connections across deeper, middle, and superficial cortical depths (Fig. 1).

Using this framework, we computed functional connectivity between V3A, earlier (i.e., V1), and higher (i.e., V7) visual areas involved in disparity processing. We employed an informational connectivity analysis (Coutanche and Thompson-Schill, 2014; Anzellotti and Coutanche, 2018; Koster et al., 2018; Jia et al., 2020) and tested whether these regions shared synchronous discriminability of multivoxel patterns related to disparity processing. Consistent with previous studies (Rockland and Pandya, 1979; Self et al., 2013; Markov et al., 2014), we examined the following possible functional connectivity mechanisms (Lawrence et al., 2019b): (1) feedforward processing, as indicated by functional connectivity between superficial and middle layers between earlier and higher visual areas, and (2) feedback processing, as indicated by functional connectivity between deeper layers across areas. We did not test connectivity between superficial layers and deeper layers across areas, as it is known to relate to both feedforward and feedback processing (Fig. 1; Rockland and Pandya, 1979; Maunsell and van Essen, 1983).

To understand functional connectivity mechanisms that relate to stereoscopic perception, we focused on differences in the information flow for correlated versus anticorrelated stimuli rather than overall differences in feedforward versus feedback processing. We reasoned that stronger connectivity for correlated stimuli supports stereoscopic perception and tested whether this functional connectivity involves feedback versus feedforward processes. To this end, we tested differences in functional connectivity between correlated versus anticorrelated stimuli in feedforward and feedback pathways. Following previous studies using an informational connectivity analysis (Koster et al., 2018; Jia et al., 2020), we interrogated the MVPA classifiers for each layer and extracted the distance from the hyperplane for the mean pattern signal per block. For each layer per ROI we generated a time course of distance values across blocks and calculated the Spearman correlation between layers across blocks for correlated versus anticorrelated stimuli (Fig. 6A). Our results showed that functional connectivity for correlated versus anticorrelated stimuli involves (1) feedforward processing between V3A and V7 and (2) feedback processing from V3A to V1 and from V7 to V3A.

In particular, we showed higher feedforward connectivity between V3A and V7 for correlated than anticorrelated stimuli. A repeated-measures ANOVA (condition × ROI pair) on the correlation coefficients (Fisher's *z*) showed a significant main effect of condition ($F_{(1,6)} = 9.47$, $p = 0.022$, Fig. 6B), main effect of ROI pair ($F_{(2,12)} = 8.24$, $p = 0.006$), and a significant condition × ROI pair interaction ($F_{(2,12)} = 3.92$, $p = 0.049$). *Post hoc* comparison showed higher connectivity for correlated than anticorrelated stimuli between superficial layers of V3A and middle layers of V7 ($t_{(6)} = 6.46$, $p = 0.001$), suggesting that signals related to stereoscopic perception are computed in V3A and fed forward to V7. No significant differences were observed in feedforward connectivity between V1 and V3A ($t_{(6)} = 1.35$, $p = 0.222$) nor between V1 and V7 ($t_{(6)} = -0.51$, $p = 0.630$).

Further, we showed higher feedback connectivity between V3A and V1 and V7 and V3A for correlated than anticorrelated stimuli. A repeated-measures ANOVA (condition × ROI pair) on the correlation coefficients (Fisher's *z*) showed significant main effect of condition ($F_{(1,6)} = 8.31$, $p = 0.028$; Fig. 6B) and a significant condition × ROI pair interaction ($F_{(2,12)} = 6.76$, $p = 0.011$) but no significant main effect of ROI pair ($F_{(1.1,6.5)} = 0.29$, $p = 0.627$). *Post hoc* comparison showed (1) higher connectivity for correlated than anticorrelated stimuli between deeper layers of V1 and V3A ($t_{(6)} = 2.76$, $p = 0.032$), suggesting that signals related to stereoscopic perception are computed in V3A and fed back to the primary visual cortex, and (2) higher connectivity for correlated than anticorrelated stimuli between deeper layers of V3A and V7 ($t_{(6)} = 5.03$, $p = 0.003$), suggesting that signals are related to stereoscopic perception in V7 and fed back to V3A. No significant differences were observed in feedback connectivity between V1 and V7 ($t_{(6)} = -0.5$, $p = 0.635$).

Discussion

Here, we capitalize on the submillimeter resolution of 7T laminar fMRI to interrogate the circuit processes (feedforward, feedback) that underlie 3D perception. Our results indicate that area V3A is a key nexus for the processing of stereoscopic signals that are propagated to higher dorsal visual areas (V7) and then fed back to the primary visual cortex to support 3D perception.

Combining 7T imaging with MVPA, we demonstrate a role of dorsal areas (V3A, V7) in 3D perception, consistent with previous fMRI studies showing (1) disparity-evoked fMRI responses in V1, V3A, and V7 (Bridge and Parker, 2007; Preston et al., 2008; Goncalves et al., 2015; Rideaux and Welchman, 2019; Nasr and Tootell, 2020) and (2) discriminable multivoxel fMRI pattern responses to disparity-defined position (i.e., near vs far planes) in V3A (Preston et al., 2008; Goncalves et al., 2015; Patten and Welchman, 2015; Li et al., 2017; Liu et al., 2020). Our fMRI results extend beyond these previous studies by demonstrating layer-specific representations related to stereoscopic perception in V3A and V7 (i.e., higher MVPA accuracy for correlated than anticorrelated stimuli in upper than deeper layers). Despite the relatively small sample size ($N = 8$) in this study, a series of control analyses corroborated our results showing that they are not dependent on methodological choices (e.g., V7 definition, classification methods for decoding, voxel pattern size).

We interpret our results within a framework of feedforward and feedback connectivity across cortical depths (Fig. 1*A*), as proposed by previous UHF imaging studies (Kok et al., 2016; Huber et al., 2017; Sharoh et al., 2019; Moerel et al., 2020). In particular, sensory inputs are known to enter the cortex at the level of the middle layer (layer 4), and output information is fed forward through the superficial layers (layer 2/3). In contrast, feedback information is thought to be exchanged between (1) deeper layers between visual areas (layer 5/6) and (2) deeper layers in higher visual areas and superficial layers in lower visual areas (Larkum, 2013; Markov et al., 2014). Previous work has shown that synaptic input to superficial layers may be because of an increase in feedback signals carried by neurons that have dendrites projecting to the superficial layers and their cell bodies in deeper layers (Larkum, 2013). Recent UHF brain imaging studies in animals and humans provide converging evidence for this information flow profile across species (Huber et al., 2021; Jung et al., 2021). Further, neurophysiological studies have shown that this micro circuit is involved in a range of visual recognition (Self et al., 2013; van Kerkoerle et al., 2014) and attention (Buffalo et al., 2011) tasks. Recent laminar fMRI studies provide evidence for the involvement of this circuit in the context of sensory processing (De Martino et al., 2015; Muckli et al., 2015; Gau et al., 2020; Jia et al., 2020; Zamboni et al., 2020) and visual attention (Fracasso et al., 2016; Scheeringa et al., 2016; Lawrence et al., 2019a). Thus, our results showing layer-specific representations related to stereoscopic perception in upper rather than deeper layers of V3A and V7 suggest that these regions are involved in the processing of input disparity signals and their read out in support of 3D perception.

Next, we interrogated the layer-to-layer functional connectivity between V3A and earlier (i.e., V1) or higher (i.e., V7) visual areas that allows us to test feedforward and feedback processing based on known anatomic connectivity models (Self et al., 2013; Markov et al., 2014; Lawrence et al., 2019a). First, we demonstrate stronger feedforward connectivity for correlated stimuli between superficial layers of V3A and middle layers of V7 and feedback connectivity between deeper layers in these areas. These results suggest that processing of disparity-specific information in V3A involves both feedforward and feedback processes that contribute to 3D perception. These results are consistent with pervious monkey electrophysiology studies showing a functional link between V3A and a homolog region to human V7 (Nakamura et al., 2001) for processing disparity-defined stimuli. Further work using electrophysiology methods that provide high temporal resolution is necessary to understand the timings of feedforward and feedback processes and how they contribute to 3D perception.

Second, we demonstrate feedback connectivity specific to stereoscopic perception (i.e., stronger connectivity for correlated than anticorrelated stimuli) between deeper V1 and V3A layers, suggesting top-down influences to disparity processing in the primary visual cortex through feedback from higher visual dorsal areas known to be involved in stereo vision and disparity (Goncalves et al., 2015; Nasr and Tootell, 2020). Previous neurophysiology studies have shown attenuated responses in V1 for anticorrelated compared with correlated stimuli (Cumming and Parker, 1997; Samonds et al., 2013). Further, disparity tuning curves of many neurons that respond to anticorrelated stimuli have been shown to be inverted and attenuated compared with the typical responses to correlated stimuli, a possible suppression mechanism in V1 that aids 3D perception (Goncalves and Welchman, 2017). Our functional connectivity results suggest that stronger neural responses for correlated than anticorrelated stimuli in V1 may reflect feedback from higher dorsal visual areas (i.e., V3A) to deeper V1 layers. Previous fMRI studies (Bridge and Parker, 2007; Preston et al., 2008) at standard resolution do not report differences in fMRI responses to correlated versus anticorrelated stimuli in V1. In contrast, UHF imaging provides the submillimeter resolution to capture these differences using MVPA and reveals the fine-scale processes (i.e., feedback) that contribute to 3D perception.

These findings advance our understanding of the mechanisms involved in 3D perception at a finer scale by suggesting a flow of information between the primary visual cortex and higher portions of the dorsal visual cortex involved in processing stereoscopic stimuli. Although it is clear that anticorrelated stimuli drive responses in the primary visual cortex (Cumming and Parker, 1997), responses are attenuated, which may reflect the influence of feedback signals from higher visual processing (e.g., V3A). Individual anticorrelated signals per se may be useful in supporting perceptual judgments (Goncalves and Welchman, 2017); however, it is clear that a whole display of aRDS does not provide any stable impression of 3D structures, which may drive feedback signals to modulate the activity of disparity-selective neurons in V1 that represent the first stage of binocular processing in the visual system. The use of time-resolved techniques (e.g., MEG, EEG) in addition to laminar specificity may help unpick the functional role of this activity in future work.

It is important to note that despite the advances provided by UHF imaging, GE-EPI remains limited by vasculature-related signals contributing to BOLD at the cortical surface, resulting in loss of spatial specificity (Kashyap et al., 2018; Kay et al., 2019). To reduce this superficial bias, we removed voxels with low tSNR (Olman et al., 2007) and high *t* statistic for stimulation contrast (Polimeni et al., 2010; Kashyap et al., 2018). Further, we applied a signal unmixing method (Kok et al., 2016; Koster et al., 2018) as a control analysis for draining vein effects from middle to superficial layers. We have previously shown that these corrections return the BOLD signal across cortical depths comparable to that recorded using a 3D gradient and spin echo sequence, which is known to be sensitive to signals from small vessels and less affected by larger veins, resulting in higher spatial specificity of the measured BOLD signal (De Martino et al., 2013; Kemper et al., 2015; Zamboni et al., 2020). Finally, we compared BOLD signals across stimulus conditions and cortical depths after *z*-scoring the signals within each cortical depth to account for possible differences in signal strength across cortical layers (Goense et al., 2012; Havlicek and Uludağ, 2020). Following these corrections, we observed layer-specific differences in MVPA accuracy for correlated compared with anticorrelated stimuli, suggesting that our results are unlikely to be confounded by vasculature-related superficial bias. Our results are consistent with previous laminar imaging studies showing BOLD effects in superficial layers in a range of tasks (De Martino et al., 2015; Muckli et al., 2015; Lawrence et al., 2019a; Gau et al., 2020; Jia et al., 2020) and could not be simply attributed to differences in attention because of task difficulty as participants engaged in an attentionally demanding task across conditions. Although we used a series of analyses to control for the superficial bias, it could not be completely ruled out. Vascular space occupancy contrast (VASO) is sensitive to arteriole and postarterial cerebral blood volume (CBV) changes and shows reduced draining vein contamination compared with BOLD (Huber et al., 2019; Beckett et al., 2020). The lower functional contrast (SNR) of VASO compared with GE-EPI imaging means that longer data acquisition sessions are necessary, which may not always be possible within the timing constraints of human brain imaging studies. However, future work could capitalize on advances in CBV imaging using VASO to enhance the spatial specificity of laminar brain imaging and to control for the superficial bias at the data acquisition stage.

In sum, exploiting UHF fMRI, we provide evidence for the role of V3A in a circuit of feedforward and feedback interactions that support the processing of perceived binocular depth in the visual cortex. Interrogating these interactions at the finer resolution available with UHF imaging, we provide the first insights in bridging the gap between animal neurophysiology and human fMRI studies investigating cross-scale circuits, from micro circuits to global brain networks for 3D perception.

References

Anzellotti S, Coutanche MN (2018) Beyond functional connectivity: investigating networks of multivariate representations. Trends Cogn Sci 22:258–269.

Backus BT, Fleet DJ, Parker AJ, Heeger DJ (2001) Human cortical activity correlates with stereoscopic depth perception. J Neurophysiol 86:2054–2068.

Beckett AJS, Dadakova T, Townsend J, Huber L, Park S, Feinberg DA (2020) Comparison of BOLD and CBV using 3D EPI and 3D GRASE for cortical layer functional MRI at 7 T. Magn Reson Med 84:3128–3145.

Benson NC, Butt OH, Datta R, Radoeva PD, Brainard DH, Aguirre GK (2012) The retinotopic organization of striate cortex is well predicted by surface topology. Curr Biol 22:2081–2085.

Benson NC, Butt OH, Brainard DH, Aguirre GK (2014) Correction of distortion in flattened representations of the cortical surface allows prediction of V1-V3 functional organization from anatomy. PLoS Comput Biol 10: e1003538.

Benson NC, Jamison KW, Arcaro MJ, Vu AT, Glasser MF, Coalson TS, Van Essen DC, Yacoub E, Ugurbil K, Winawer J, Kay K (2018) The Human Connectome Project 7 Tesla retinotopy dataset: description and population receptive field analysis. J Vis 18:23.

Blasdel GG, Lund JS (1983) Termination of afferent axons in macaque striate cortex. J Neurosci 3:1389–1413.

Brainard DH (1997) The psychophysics toolbox. Spat Vis 10:433–436.

Bridge H, Parker AJ (2007) Topographical representation of binocular depth in the human visual cortex using fMRI. J Vis 7(14):15. 1–14.

Buffalo EA, Fries P, Landman R, Buschman TJ, Desimone R (2011) Laminar differences in gamma and alpha coherence in the ventral stream. Proc Natl Acad Sci U S A 108:11262–11267.

Chang C-C, Lin C-J (2011) LIBSVM: a library for support vector machines. ACM Trans Intell Syst Technol 2:1–27.

Cottereau BR, McKee SP, Ales JM, Norcia AM (2011) Disparity-tuned population responses from human visual cortex. J Neurosci 31:954–965.

Cottereau BR, Ales JM, Norcia AM (2014) The evolution of a disparity decision in human visual cortex. Neuroimage 92:193–206.

Coutanche MN, Thompson-Schill SL (2014) Fast mapping rapidly integrates information into existing memory networks. J Exp Psychol Gen 143:2296–2303.

Cumming BG, Parker AJ (1997) Responses of primary visual cortical neurons to binocular disparity without depth perception. Nature 389:280–283.

De Martino F, Zimmermann J, Muckli L, Ugurbil K, Yacoub E, Goebel R (2013) Cortical depth dependent functional responses in humans at 7T: improved specificity with 3D GRASE. PLoS One 8:e60514.

De Martino F, Moerel M, Ugurbil K, Goebel R, Yacoub E, Formisano E (2015) Frequency preference and attention effects across cortical depths in the human primary auditory cortex. Proc Natl Acad Sci U S A 112:16036–16041.

Diedrichsen J, Provost S, Zareamoghaddam H (2016) On the distribution of cross-validated Mahalanobis distances. arXiv:1607.01371.

Duvernoy HM, Delon S, Vannson JL (1981) Cortical blood vessels of the human brain. Brain Res Bull 7:519–579.

Engel SA, Glover GH, Wandell BA (1997) Retinotopic organization in human visual cortex and the spatial precision of functional MRI. Cereb Cortex 7:181–192.

Fischl B (2012) FreeSurfer. Neuroimage 62:774–781.

Fracasso A, Petridou N, Dumoulin SO (2016) Systematic variation of population receptive field properties across cortical depth in human visual cortex. Neuroimage 139:427–438.

Gau R, Bazin P-L, Trampel R, Turner R, Noppeney U (2020) Resolving multisensory and attentional influences across cortical depth in sensory cortices. Elife 9:e46856.

Goense J, Merkle H, Logothetis NK (2012) High-resolution fMRI reveals laminar differences in neurovascular coupling between positive and negative BOLD responses. Neuron 76:629–639.

Goense J, Bohraus Y, Logothetis NK (2016) fMRI at high spatial resolution: implications for BOLD-models. Front Comput Neurosci 10:66.

Goncalves NR, Welchman AE (2017) "What not" detectors help the brain see in depth. Curr Biol 27:1403–1412.e8.

Goncalves NR, Ban H, Sánchez-Panchuelo RM, Francis ST, Schluppeck D, Welchman AE (2015) 7 tesla fMRI reveals systematic functional organization for binocular disparity in dorsal visual cortex. J Neurosci 35:3056–3072.

Greve DN, Fischl B (2009) Accurate and robust brain image alignment using boundary-based registration. Neuroimage 48:63–72.

Havlicek M, Uludağ K (2020) A dynamical model of the laminar BOLD response. Neuroimage 204:116209.

Hubel DH, Wiesel TN (1972) Laminar and columnar distribution of geniculo-cortical fibers in the macaque monkey. J Comp Neurol 146:421–450.

Huber L, Handwerker DA, Jangraw DC, Chen G, Hall A, Stüber C, Gonzalez-Castillo J, Ivanov D, Marrett S, Guidi M, Goense J, Poser BA, Bandettini PA (2017) High-resolution CBV-fMRI allows mapping of laminar activity and connectivity of cortical input and output in human M1. Neuron 96:1253–1263.e7.

Huber L, Uludağ K, Möller HE (2019) Non-BOLD contrast for laminar fMRI in humans: CBF, CBV, and CMRO2. Neuroimage 197:742–760.

Huber L, Poser BA, Kaas AL, Fear EJ, Dresbach S, Berwick J, Goebel R, Turner R, Kennerley AJ (2021) Validating layer-specific VASO across species. Neuroimage 237:118195.

Ip IB, Minini L, Dow J, Parker AJ, Bridge H (2014) Responses to interocular disparity correlation in the human cerebral cortex. Ophthalmic Physiol Opt 34:186–198.

Janssen P, Vogels R, Liu Y, Orban GA (2003) At least at the level of inferior temporal cortex, the stereo correspondence problem is solved. Neuron 37:693–701.

Jia K, Zamboni E, Kemper VG, Rua C, Goncalves NR, Ng AKT, Rodgers CT, Williams G, Goebel R, Kourtzi Z (2020) Recurrent processing drives perceptual plasticity. Curr Biol 30:4177–4187.e4.

Jung WB, Im GH, Jiang H, Kim S-G (2021) Early fMRI responses to somatosensory and optogenetic stimulation reflect neural information flow. Proc Natl Acad Sci U S A 118:e2023265118.

Kashyap S, Ivanov D, Havlicek M, Poser BA, Uludağ K (2018) Impact of acquisition and analysis strategies on cortical depth-dependent fMRI. Neuroimage 168:332–344.

Kay K, Jamison KW, Vizioli L, Zhang R, Margalit E, Ugurbil K (2019) A critical assessment of data quality and venous effects in sub-millimeter fMRI. Neuroimage 189:847–869.

Kemper VG, De Martino F, Vu AT, Poser BA, Feinberg DA, Goebel R, Yacoub E (2015) Sub-millimeter T2 weighted fMRI at 7 T: Comparison of 3D-GRASE and 2D SE-EPI. Front Neurosci 9:163.

Kemper VG, De Martino F, Emmerling TC, Yacoub E, Goebel R (2018) High resolution data analysis strategies for mesoscale human functional MRI at 7 and 9.4T. Neuroimage 164:48–58.

Kok P, Bains Lauren J, van Mourik T, Norris DG, de Lange FP (2016) Selective activation of the deep layers of the human primary visual cortex by top-down feedback. Curr Biol 26:371–376.

Koster R, Chadwick MJ, Chen Y, Berron D, Banino A, Düzel E, Hassabis D, Kumaran D (2018) Big-loop recurrence within the hippocampal system supports integration of information across episodes. Neuron 99:1342–1354.e6.

Larkum M (2013) A cellular mechanism for cortical associations: an organizing principle for the cerebral cortex. Trends Neurosci 36:141–151.

Lawrence SJD, Norris DG, de Lange FP (2019a) Dissociable laminar profiles of concurrent bottom-up and top-down modulation in the human visual cortex. Elife 8:e44422.

Lawrence SJD, Formisano E, Muckli L, de Lange FP (2019b) Laminar fMRI: applications for cognitive neuroscience. Neuroimage 197:785–791.

Li Y, Zhang C, Hou C, Yao L, Zhang J, Long Z (2017) Stereoscopic processing of crossed and uncrossed disparities in the human visual cortex. BMC Neurosci 18:80.

Liu C, Li Y, Song S, Zhang J (2020) Decoding disparity categories in 3-dimensional images from fMRI data using functional connectivity patterns. Cogn Neurodyn 14:169–179.

Livingstone MS, Hubel DH (1984) Anatomy and physiology of a color system in the primate visual cortex. J Neurosci 4:309–356.

Markov NT, Vezoli J, Chameau P, Falchier A, Quilodran R, Huissoud C, Lamy C, Misery P, Giroud P, Ullman S, Barone P, Dehay C, Knoblauch K, Kennedy H (2014) Anatomy of hierarchy: feedforward and feedback pathways in macaque visual cortex. J Comp Neurol 522:225–259.

Markuerkiaga I, Barth M, Norris DG (2016) A cortical vascular model for examining the specificity of the laminar BOLD signal. Neuroimage 132:491–498.

Marquardt I, Schneider M, Gulban OF, Ivanov D, Uludağ K (2018) Cortical depth profiles of luminance contrast responses in human V1 and V2 using 7 T fMRI. Hum Brain Mapp 39:2812–2827.

Maunsell JH, van Essen DC (1983) The connections of the middle temporal visual area (MT) and their relationship to a cortical hierarchy in the macaque monkey. J Neurosci 3:2563–2586.

Minini L, Parker AJ, Bridge H (2010) Neural modulation by binocular disparity greatest in human dorsal visual stream. J Neurophysiol 104:169–178.

Moeller S, Yacoub E, Olman CA, Auerbach E, Strupp J, Harel N, Uğurbil K (2010) Multiband multislice GE-EPI at 7 tesla, with 16-fold acceleration using partial parallel imaging with application to high spatial and temporal whole-brain fMRI. Magn Reson Med 63:1144–1153.

Moerel M, Yacoub E, Gulban OF, Lage-Castellanos A, De Martino F (2020) Using high spatial resolution fMRI to understand representation in the auditory network. Prog Neurobiol. Advance online publication. Retrieved Aug 1, 2020. doi: 10.1016/j.pneurobio.2020.101887.

Muckli L, De Martino F, Vizioli L, Petro LS, Smith FW, Ugurbil K, Goebel R, Yacoub E (2015) Contextual feedback to superficial layers of V1. Curr Biol 25:2690–2695.

Murphy AP, Ban H, Welchman AE (2013) Integration of texture and disparity cues to surface slant in dorsal visual cortex. J Neurophysiol 110:190–203.

Nakamura H, Kuroda T, Wakita M, Kusunoki M, Kato A, Mikami A, Sakata H, Itoh K (2001) From three-dimensional space vision to prehensile hand movements: the lateral intraparietal area links the area V3A and the anterior intraparietal area in macaques. J Neurosci 21:8174–8187.

Nasr S, Tootell RBH (2018) Visual field biases for near and far stimuli in disparity selective columns in human visual cortex. Neuroimage 168:358–365.

Nasr S, Tootell RBH (2020) Asymmetries in global perception are represented in near- versus far-preferring clusters in human visual cortex. J Neurosci 40:355–368.

O'Brien F, Cousineau D (2014) Representing error bars in within-subject designs in typical software packages. Quant Methods Psychol 10:56–67.

Olman CA, Inati S, Heeger DJ (2007) The effect of large veins on spatial localization with GE BOLD at 3 T: displacement, not blurring. Neuroimage 34:1126–1135.

Parker AJ, Coullon GSL, Sánchez-Panchuelo RM, Francis ST, Clare S, Kay DA, Duff EP, Minini L, Jbabdi S, Schluppeck D, Bridge H (2017) Geospatial statistics of high field functional MRI reveals topographical clustering for binocular stereo depth in early visual cortex. bioRxiv 160788..

Patten ML, Welchman AE (2015) fMRI activity in posterior parietal cortex relates to the perceptual use of binocular disparity for both signal-in-noise and feature difference tasks. PLoS One 10:e0140696.

Pelli DG (1997) The VideoToolbox software for visual psychophysics: transforming numbers into movies. Spat Vis 10:437–442.

Polimeni JR, Fischl B, Greve DN, Wald LL (2010) Laminar analysis of 7T BOLD using an imposed spatial activation pattern in human V1. Neuroimage 52:1334–1346.

Popple AV, Smallman HS, Findlay JM (1998) The area of spatial integration for initial horizontal disparity vergence. Vision Res 38:319–326.

Preston TJ, Li S, Kourtzi Z, Welchman AE (2008) Multivoxel pattern selectivity for perceptually relevant binocular disparities in the human brain. J Neurosci 28:11315–11327.

Rideaux R, Welchman AE (2019) Contextual effects on binocular matching are evident in primary visual cortex. Vision Res 159:76–85.

Rockland KS, Pandya DN (1979) Laminar origins and terminations of cortical connections of the occipital lobe in the rhesus monkey. Brain Res 179:3–20.

Samonds JM, Potetz BR, Tyler CW, Lee TS (2013) Recurrent connectivity can account for the dynamics of disparity processing in V1. J Neurosci 33:2934–2946.

Scharstein D, Szeliski R (2002) A taxonomy and evaluation of dense two-frame stereo correspondence algorithms. Int J Comput Vis 47:7–42.

Scheeringa R, Koopmans PJ, van Mourik T, Jensen O, Norris DG (2016) The relationship between oscillatory EEG activity and the laminar-specific BOLD signal. Proc Natl Acad Sci U S A 113:6761–6766.

Self MW, van Kerkoerle T, Supèr H, Roelfsema PR (2013) Distinct roles of the cortical layers of area V1 in figure-ground segregation. Curr Biol 23:2121–2129.

Self MW, van Kerkoerle T, Goebel R, Roelfsema PR (2019) Benchmarking laminar fMRI: neuronal spiking and synaptic activity during top-down and bottom-up processing in the different layers of cortex. Neuroimage 197:806–817.

Sereno MI, Dale AM, Reppas JB, Kwong KK, Belliveau JW, Brady TJ, Rosen BR, Tootell RBH (1995) Borders of multiple visual areas in humans revealed by functional magnetic resonance imaging. Science 268:889–893.

Sharoh D, van Mourik T, Bains LJ, Segaert K, Weber K, Hagoort P, Norris DG (2019) Laminar specific fMRI reveals directed interactions in distributed networks during language processing. Proc Natl Acad Sci U S A 116:21185–21190.

Tanabe S, Cumming BG (2014) Delayed suppression shapes disparity selective responses in monkey V1. J Neurophysiol 111:1759–1769.

Tootell RBH, Nasr S (2017) Columnar segregation of magnocellular and parvocellular streams in human extrastriate cortex. J Neurosci 37:8014–8032.

Tsao DY, Vanduffel W, Sasaki Y, Fize D, Knutsen TA, Mandeville JB, Wald LL, Dale AM, Rosen BR, Van Essen DC, Livingstone MS, Orban GA, Tootell RBH (2003) Stereopsis activates V3A and caudal intraparietal areas in macaques and humans. Neuron 39:555–568.

Uğurbil K, Toth L, Kim D-S (2003) How accurate is magnetic resonance imaging of brain function? Trends Neurosci 26:108–114.

Uludağ K, Müller-Bierl B, Uğurbil K (2009) An integrative model for neuronal activity-induced signal changes for gradient and spin echo functional imaging. Neuroimage 48:150–165.

van Kerkoerle T, Self MW, Dagnino B, Gariel-Mathis M-A, Poort J, van der Togt C, Roelfsema PR (2014) Alpha and gamma oscillations characterize feedback and feedforward processing in monkey visual cortex. Proc Natl Acad Sci U S A 111:14332–14341.

Waehnert MD, Dinse J, Weiss M, Streicher MN, Waehnert P, Geyer S, Turner R, Bazin P-L (2014) Anatomically motivated modeling of cortical laminae. Neuroimage 93 Pt 2:210–220.

Walther A, Nili H, Ejaz N, Alink A, Kriegeskorte N, Diedrichsen J (2016) Reliability of dissimilarity measures for multi-voxel pattern analysis. Neuroimage 137:188–200.

Wang L, Mruczek REB, Arcaro MJ, Kastner S (2015) Probabilistic maps of visual topography in human cortex. Cereb Cortex 25:3911–3931.

Welchman AE (2016) The human brain in depth: how we see in 3D. Annu Rev Vis Sci 2:345–376.

Yacoub E, Van De Moortele P-F, Shmuel A, Uğurbil K (2005) Signal and noise characteristics of Hahn SE and GE BOLD fMRI at 7 T in humans. Neuroimage 24:738–750.

Yushkevich PA, Piven J, Hazlett HC, Smith RG, Ho S, Gee JC, Gerig G (2006) User-guided 3D active contour segmentation of anatomical structures: significantly improved efficiency and reliability. Neuroimage 31:1116–1128.

Zamboni E, Kemper VG, Goncalves NR, Jia K, Karlaftis VM, Bell SJ, Giorgio J, Rideaux R, Goebel R, Kourtzi Z (2020) Fine-scale computations for adaptive processing in the human brain. Elife 9:e57637.